ARTICLE   OPEN

Check for updates

NSD1 supports cell growth and regulates autophagy in HPV-negative head and neck squamous cell carcinoma

Iuliia Topchu [1], Igor Bychkov[1,2], Demirkan Gursel[3], Petr Makhov [2] and Yanis Boumber [1,4 ✉]

Head and neck squamous cell carcinoma (HNSCC) is the sixth most common cancer worldwide. Despite advances in therapeutic management and immunotherapy, the 5-year survival rate for head and neck cancer remains at ~66% of all diagnosed cases. A better definition of drivers of HPV-negative HNSCC that are targetable points of tumor vulnerability could lead to significant clinical advances. NSD1 is a histone methyltransferase that catalyzes histone H3 lysine 36 di-methylation (H3K36me^2); mutations inactivating NSD1 have been linked to improved outcomes in HNSCC. In this study, we show that NSD1 induces H3K36me^2 levels in HNSCC and that the depletion of NSD1 reduces HNSCC of cell growth in vitro and in vivo. We also find that NSD1 strongly promotes activation of the Akt/mTORC1 signaling pathway. NSD1 depletion in HNSCC induces an autophagic gene program activation, causes accumulation of the p62 and LC3B-II proteins, and decreases the autophagic signaling protein ULK1 at both protein and mRNA levels. Reflecting these signaling defects, the knockdown of NSD1 disrupts autophagic flux in HNSCC cells. Taken together, these data identify positive regulation of Akt/mTORC1 signaling and autophagy as novel NSD1 functions in HNSCC, suggesting that NSD1 may be of value as a therapeutic target in this cancer.

INTRODUCTION

Head and neck cancer squamous cell carcinomas (HNSCC) arise from the mucosal epithelium and develop predominantly in the oral cavity, pharynx, and larynx [1]. HNSCC is the sixth most common cancer worldwide, with about 900,000 new cases annually [2], including more than 60,000 in the United States [3]. In the United States, approximately 4% of the US population will be diagnosed with HNSCC, and 15,000 die from this disease each year, representing a significant healthcare problem [4]. Despite advances in therapeutic management and immunotherapy, the 5-year survival rate for head and neck cancer remains at 59–76% of all diagnosed cases; for disease diagnosed at an advanced stage, 5-year survival is 34–49% depending on types of head and neck cancer [4]. Factors such as smoking and alcohol consumption are strongly associated with the risk of HNSCC, while a growing number of cases are caused by infection with human papilloma-viruses (HPVs) [5]. HPV-positive HNSCC patients have a more favorable prognosis than HPV-negative patients [1], while HPV-negative HNSCC is associated with much worse outcomes [6]. A better definition of the targetable oncogenic mechanisms of HPV-negative HNSCC could lead to significant clinical advances.

Deregulation of histone methylation, including lysine 36 dimethylation (K36me^2) of histone H3, is sometimes detected during tumor development and progression [7]. NSD1, NSD2, and NSD3 are key histone methyltransferases (HMTs) that catalyze mono- and dimethylation of H3K36 [8]. Depletion of NSD1 is associated with DNA hypomethylation in HNSCC cells [9, 10], and

NSD1 depletion usually leads to a significant reduction of the level of H3K36me^2 at the intergenic genomic regions [11]. *NSD1* inactivating mutations have been reported to occur at a frequency of 10–13% and correlate with a better prognosis for HNSCC patients [9, 12, 13], especially among patients with HPV-negative laryngeal tumors [9], in the analysis of a cohort of patients in which treatment with chemoradiation was common.

Besides these global chromatin effects related to HMT activity, it has been demonstrated in other cancer types that NSD1 regulates additional oncogenic signaling pathways, such as nuclear factor-kappa B (NF-κB) [14], Wnt/β-catenin [15, 16], and HIF1α [17]. NSD1 loss decreases the growth of liver, breast and esophageal cancer cells [15–17], and NSD1 depletion leads to a moderate increase in sensitivity to cisplatin and carboplatin drugs [12, 13]. However, non-tumorigenic human keratinocytes also have increased sensitivity to DNA-damaging agents after NSD1 depletion, which is suggestive of NSD1 regulation of this process not only in cancer, but also in normal cells [12]. Immune checkpoint inhibitors are showing great promise in numerous tumor types; however, HNSCC tumors with inactivating *NSD1* mutations have an "immune cold" microenvironment, characterized by the reduced infiltration by tumor-associated leukocytes [18]. Further, a recent publication has used multiple in vivo and in vitro models to show that depletion of NSD1 leads to tumor immune evasion in HNSCC [19]. Based on these results, it has been suggested that *NSD1*-mutated tumors may be less sensitive to immunotherapy, although data directly supporting this idea and details of the

---

[1]Robert H. Lurie Comprehensive Cancer Center, Feinberg School of Medicine, Division of Hematology/Oncology, Northwestern University, Chicago, IL 60611, USA. [2]Cancer Signaling and Microenvironment Program, Fox Chase Cancer Center, Philadelphia, PA 19111, USA. [3]Pathology Core Facility, Feinberg School of Medicine, Northwestern University, Chicago, IL 60611, USA. [4]Division of Hematology/Oncology, Sections of Thoracic / Head and Neck Medical Oncology, O'Neal Comprehensive Cancer Center, Heersink School of Medicine, University of Alabama in Birmingham, Birmingham, AL 35233, USA. ✉email: yboumber@uab.edu

underlying mechanism are not yet available [18, 20]. Overall, the mechanism by which NSD1 regulates cancer cell growth and therapeutic response is complex, and not fully understood.

The serine/threonine kinase mammalian target of rapamycin (mTOR) is a key regulator of cellular metabolism and a key driver of proliferation for many types of cancer [21]. Activation of the PI3K-Akt-mTOR pathway occurs in the majority of HNSCC cases and contributes to tumor growth [22–24]. The mTOR kinase is a core constituent of two protein complexes mTORC1 and mTORC2. mTORC1 promotes cell growth through the activation of the translation regulator S6 kinase (S6K), which in turn promotes protein synthesis [21]. mTORC1 also inhibits autophagy [25], a process of recycling cell components that is usually considered as a protective mechanism for cancer cells growing in nutrient poor conditions that induce metabolic stress [26]. mTOR inhibition through small molecule drugs typically initiates autophagy [25].

In this study, we have found that the striking reduction of HNSCC growth in vitro and in vivo induced by NSD1 depletion is accompanied by repression of the Akt/mTORC1 pathway. While this would normally induce autophagy, NSD1 knockdown blocks of the initial stages of autophagy through suppression of the expression of ULK1 protein, and disrupts autophagic flux, as reflected by although p62 and LC3B accumulation. These and other data suggest a dual role of the NSD1 protein in autophagy regulation: inhibition through the support of the mTORC1 pathway and activation of initial stages of autophagy via support of ULK1 expression. This work highlights a previously unsuspected role of NSD1 in control of cell growth and autophagy in cancer.

RESULTS
NSD1 regulates H3K36me2 level along with cell proliferation and tumor growth in HNSCC

First, we evaluated the NSD1 and H3K36me^2 in human normal epithelial tissues and in primary HNSCC samples. Tissue microarrays (TMAs) using with HNSCC tumor tissues derived from 36 HPV-negative patients revealed that both NSD1 and H3K36me^2 protein expression were significantly lower in normal epithelium tissues compared to HNSCC tumor tissues of stages II through IV (Fig. 1A, B).

Next, we examined the baseline expression levels of NSD1 and H3K36me^2 in six HPV-negative HNSCC cell lines. The western blot quantification showed that the highest level of NSD1 protein is in the FaDu cell line and demonstrated the highest H3K36me^2 level compared to other cell lines, while the SCC4 cell line carrying a frameshift loss-of-function mutation of NSD1 had the lowest level both NSD1 and H3K36me^2 (Supplementary Table 1, Fig. 1C, D). mRNA expression level of NSD1 was also decreased in SCC4 cells compared to other HNSCC cells (Supplementary Fig. S1A). NSD1 has two structural and functional paralogs with partially redundant function: NSD2 and NSD3 [8]. Therefore, we analyzed whether NSD2 and NSD3 mRNA and protein levels may correlate with NSD1 expression levels in these cell lines. As demonstrated in Supplementary Fig. S1B–D, there was no such correlation indicating the fact that NSD1/2/3 proteins express independently of each other in HNSCC.

We then evaluated proliferation rate in six HNSCC cell lines. Figure 1E demonstrates that SCC4 had the lowest basal level of proliferation, while FaDu cells, with the highest NSD1 expression level, showed a notably high proliferation rate. Taken together these data pointed out that the NSD1 expression level may have an impact on HNSCC cells growth.

Therefore, we investigated the role of NSD1 depletion in the isogenic cell line models. Thus, we developed four HPV-negative cell line models supporting doxycycline-inducible shRNA knockdown of NSD1 (in JHU 011, JHU 022, Cal27, and FaDu cells), each using two independent shRNAs against NSD1, with corresponding control models containing an empty pLKO as an empty vector. Interestingly, NSD1 depletion in those cells resulted in dramatic decrease of the H3K36me^2 levels (Fig. 1F, G). In parallel, we confirmed that neither the mRNA nor protein expression of NSD2 and NSD3 was affected in NSD1-depleted cells, excluding possible off-target effects of the shRNAs, or potential effects of NSD1 knockdown on the expression on its paralog proteins (Supplementary Fig. S1E–G). We then evaluated the effect of NSD1 depletion on cell proliferation using CTB assay. Importantly, NSD1 knockdown resulted in potent suppression of cell growth in all four models (Fig. 1H). Clonogenic analysis also demonstrated that NSD1 loss significantly reduced the ability to form colonies (Supplementary Fig. S2A). Additionally, we have recently published that CRISPR/Cas-9 knockout of NSD1, which can be considered as a long-term NSD1 depletion, also demonstrates a cell proliferation decrease in JHU 011 and JHU 022 HNSCC cell lines [27].

Furthermore, 6 days after NSD1 knockdown, the level of apoptosis in the JHU 011 and Cal27 lines was slightly higher compared to control cells (Supplementary Fig. S2B). This points out that NSD1 loss may promote apoptosis induction in HNSCC.

Next, to expand our in vitro observations supporting our hypothesis that NSD1 activity has an important role in regulation of HNSCC cells growth, we performed in vivo studies. To analyze the effects of NSD1 knockdown, FaDu cells bearing empty pLKO vector or expressing NSD1 shRNA (sh1) were subcutaneously injected into CB17-SCID mice, and NSD1 knockdown was induced by doxycycline 5 days after tumor cell injection. Excitingly, NSD1 depletion resulted a dramatic suppression of tumor growth (Fig. 1I). We also confirmed efficient depletion of NSD1 depletion, and reduced H3K36me^2 levels, in collected tumors (Supplementary Fig. S2C, D).

Collectively, our data clearly demonstrate that NSD1 positively regulates H3K36me^2 level in HNSCC and functionally supports HNSCC cells proliferation and tumor growth, both in vitro and in vivo. We were also able to demonstrate a significant up-regulation of the levels of H3K36me^2 and NSD1 in HNSCC clinical samples compared to normal epithelial tissues.

NSD1 depletion leads to accumulation of p62 and LC3B-II proteins in HNSCC, suggesting autophagy disruption

To explore which cell signaling programs are affected by NSD1 depletion, we performed RNA sequencing (RNA-seq) in JHU 011 and Cal27 cells, comparing cells 72 h after induction of NSD1 shRNA or control. All significantly affected gene pathways were analyzed with Gene set enrichment analysis (GSEA) and presented in Supplementary Table 8. GSEA results indicated that some of the affected pathways are consistent with the previously reported effects of NSD1 loss on inflammatory response, E2F targets genes [11, 19]. Besides this, GSEA indicated that NSD1 knockdown cells upregulated gene programs related to autophagy and response to starvation program (Fig. 2A and Supplementary Fig. S3A). We decided to focus on previously unreported findings, suggesting the role of NSD1 in autophagy and starvation gene signatures.

To confirm that NSD1 depletion affects autophagy, we evaluated LC3B-II and p62 protein levels by western blot in HNSCC cell lines. LC3B-II is a commonly used autophagy marker as the amount of LC3B-II correlates with the amount of autophagosomes. p62 directly binds to the LC3B protein and is selectively degraded by autophagy, and its degradation is another used marker to evaluate autophagy activity [28]. Therefore, we decided to test LC3B-II and p62 effects upon NSD1 knockdown.

All tested cell HNSCC cell lines demonstrated a significant accumulation of LC3B-II and p62 proteins after 72 h of NSD1-knockdown (Fig. 2B, C). The IHC staining of subcutaneous FaDu tumor tissues (Fig. 1I) demonstrated potent accumulation of p62 and LC3B-II (Fig. 2D, E). Taken together, our findings suggest disruption of autophagy upon NSD1 depletion in HNSCC.
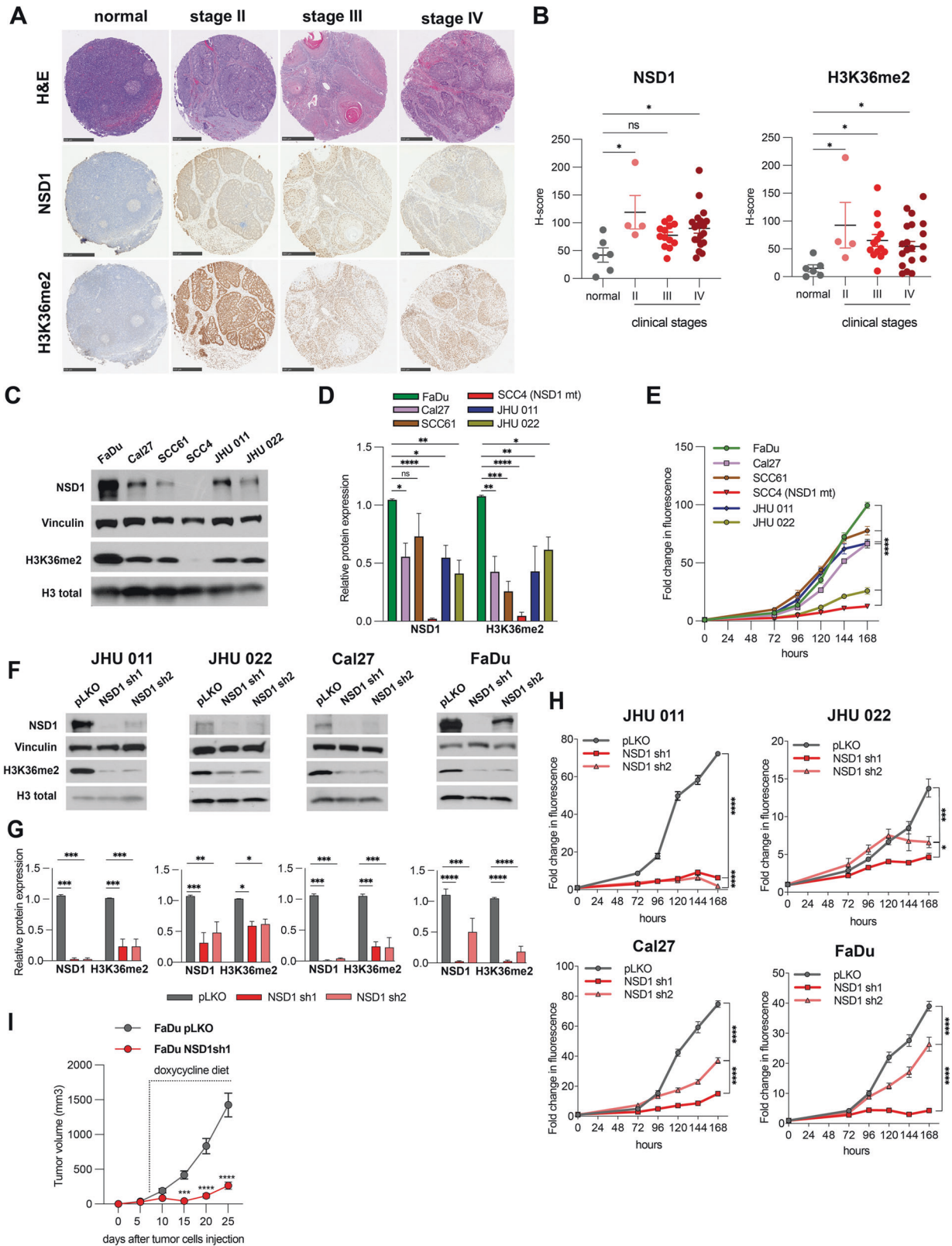
Depletion of NSD1 inhibits Akt/mTORC1 signaling pathway

Next, to explore the effects of NSD1 loss on HNSCC cell signaling pathways, we performed reverse phase protein array (RPPA) analysis in JHU 011 and Cal27 cell lines 72 h after induction of NSD1 shRNA or control (pLKO). Using RPPA, we were able to

evaluate the expression levels of total proteins and their phosphorylated isoforms for an extended study of changes in cell signaling. The full list of the detected proteins in both cell lines is presented in Supplementary Data Set 1. The RPPA data clearly demonstrated a decrease in activity of Akt/mTORC1 signaling

Fig. 1 NSD1 regulates H3K36me^2 level along with cell proliferation and tumor growth in HNSCC. A Representative images of human tumor tissues stained with NSD1 and H3K36me^2 antibody. Scale bars, 500 μm. **B** H-score calculations from (**A**). Statistical significance was determined by Kruskal–Wallis with Dunn's multiple comparisons post-test. **C** Western blot of NSD1 and H3K36me^2 levels in a panel of human head and neck cancer cell lines. **D** Quantification of Western blot images in (**C**). Statistical significance was determined by ANOVA with Dunnett multiple comparison post-test. Each group was compared to SCC4 cell line. **E** Proliferation HNSCC cell lines as measured by CTB for 168 h. Statistical significance determined by ANOVA with Dunnett multiple comparison post-test. Each group was compared to SCC4 cell line. **F** Western blot of NSD1 and H3K36me^2 protein levels in NSD1 shRNA knockdown cells at 72 h after knockdown induction. **G** Quantification of Western blot images in (**F**). Statistical significance was determined by ANOVA with Dunnett multiple comparison post-test. Each group was compared to pLKO. **H** Proliferation of pLKO-transfected or NSD1 shRNA transfected cell lines post doxycycline induction, as measured by CTB assay for up to 168 h, at indicated time points. Statistical significance was determined by ANOVA with Dunnett multiple comparison post-test. Each group was compared to pLKO. **I** Quantitation of tumor volume in mice subcutaneously injected with FaDu NSD1 knockdown cell line (FaDu pLKO as a control); $n = 8$ per group at indicated time points. Mouse number #1 from the control group died on day 23, tumor measurements were included in calculations until day 20. Statistical significance was determined by ANOVA with Šidák multiple comparison post-test. Experiments were performed in at least three independent biological repeats. The error bars are presented as mean ± SEM. ns not significant, *$p < 0.05$, **$p < 0.01$, ***$p < 0.001$, and ****$p < 0.0001$.

pathway in NSD1 depleted HNSCC cells (Fig. 3A, B). This is consistent with previously reported evidence of mTOR signaling affecting major cellular functions regulating cell growth and proliferation, and in accordance with autophagy being one of the key processes downstream of mTORC1 pathway [21]. Since NSD1 dramatically decreases cell proliferation (Fig. 1H) and leads to autophagy gene program activation (Fig. 2A), we focused on the mTORC1 pathway validation in NSD1-depleted cells.

Further validation of the RPPA data has confirmed our observations. Indeed, NSD1 knockdown reduces the activity of mTORC1 downstream signaling, as documented by decreased levels of phosphorylation levels of mTOR, p70S6K, and S6 proteins in all tested HNSCC cell lines (Fig. 3C and Supplementary Fig. S4). Given that Akt is an upstream activator of mTORC1, which stimulates mTORC1 through inhibitory phosphorylation of TSC2 (Fig. 3B) [21], we evaluated the effects of NSD1 depletion on Akt and its downstream effectors. As demonstrated in the Fig. 3D, E and Supplementary Fig. S5A, we observed a dramatic decrease of both protein and mRNA levels of Akt. Importantly, this was accompanied by the reduction of TSC2 phosphorylation (T1462). Another well-known upstream effector of TSC2 protein, p44/42 MAPK, also demonstrated significant changes in total isoform level in JHU 011, Cal27, FaDu, but not in JHU 022 cells (Supplementary Fig. S5B, C).

NSD1 affects the initial stages of autophagy through the direct regulation of ULK1 gene expression in HNSCC

Given that mTORC1 activity negatively regulates autophagy activation, we expected a mechanistic connection between downregulation of mTORC1 signaling and activation of autophagy-related gene programs upon NSD1 depletion.

The initial stages of autophagy require ULK1 protein, which phosphorylation provides the ULK complex assembly needed for autophagosome formation. Since the activity of the ULK1 has been described as the immediate event after mTORC1 pathway inactivation [29], we examined ULK1 expression after NSD1 depletion.

Surprisingly, we observed that ULK1 total protein and mRNA expression levels were reduced (Fig. 4A–C) in all tested HNSCC cell lines. This suggests the direct NSD1 control of ULK1 gene expression via H3K36me^2-dependent mechanism, as it was shown for other NSD1-regulated genes [19, 30, 31]. To understand molecular mechanism of ULK1 regulation, we performed ChIP-qPCR analysis. NSD1-depleted cells demonstrated dramatic reduction of H3K36me^2 level in the region of ULK1 promoter, suggesting direct regulation of ULK1 gene expression by NSD1 (Fig. 4D, E).

Next, we have evaluated the possible contribution of ULK1 expression in regulating HNSCC cell growth and in regulating p62 and LC3B levels. Therefore, we performed siRNA knockdown of ULK1 in JHU011 and Cal27 cell lines. We have not observed any

impact on p62 or LC3B levels or proliferation upon ULK1 knockdown (Supplementary Fig. S6A–C).

Moreover, the phosphorylation of Beclin-1 (pS30), downstream target of ULK1 [32], was decreased in NSD1-depleted cells of JHU 011 and Cal27 cell lines. The level of the total isoform of Beclin-1 was stable in the Cal27 cell line, though it significantly changed in the JHU 011 cell line under NSD1 sh1, but not in NSD1 sh2 (Fig. 4F, G). RNA-sequencing results showed a decrease in BECN1 gene which is a part of Autophagosome gene program (Supplementary Fig. S3A) in JHU 011 cell line and no changes in Cal27. This is suggestive of possible regulation by NSD1 of not only ULK1 at the transcriptional level but also of its downstream target Beclin-1 in laryngeal cancer cell types.

Given that AMPK can activate Beclin-1 by direct phosphorylating at Serine 93 [33, 34], we evaluated the potential autophagy-activating compensatory effect of AMPK upon the decrease of pS30 Beclin-1 phosphorylation caused by the downregulation of UKL1 expression.

In contrast to our expectation that AMPK activity can compensate for the loss of ULK1 and activate Beclin-1 through the pS93 phosphorylation site, we observed that pT172 AMPK was decreased along with it's total isoform in JHU 011 cell line (Fig. 4H, I). However, the decreased level mRNA expression of AMPK subunits in JHU 011 cell lines according to the RNA-sequencing data was not observed (Supplementary Fig. S3B). pS93 Beclin-1 level was reduced only in NSD1 sh1 cells in the JHU 011 cell line which can be explained by the changes of total Beclin-1 level only under NSD1 sh1 (Fig. 4F, G). Cal27 cell line did not demonstrate any change in phosphorylated and total AMPK protein levels but had a slight decrease in pS93 Beclin-1 protein (Fig. 4H, I).

Therefore, the above findings led us to the conclusion that the decrease in the ULK1 level and has not been compensated by AMPK activity, and in JHU 011 and Cal27 cells, the loss of autophagy signaling activation occurs at the ULK1/Beclin-1 level. Collectively, these results indicate that NSD1 positively directly regulates ULK1 gene expression, and that the depletion of NSD1 may promote inhibition of the autophagy cascade at the initial stages in HNSCC.

Autophagic flux is disrupted in NSD1-depleted HNSCC cells

The above findings clearly demonstrated that NSD1 depletion in HNSCC cells promoted the accumulation of p62 and LC3B-II, but also resulted in the decrease of ULK1 levels and pS30 Beclin-1 phosphorylation, which might seem to be contradictory results.

As an additional control, we decided to evaluate ULK1, p62, and LC3B-II protein changes in response to mTOR inhibition in JHU 011 and Cal27 wild-type cells, suggesting that in NSD1-depleted cells, autophagy gene program activation occurs in response to the mTORC1 signaling decrease.

We chemically inhibited mTORC1 with the clinically useful mTOR inhibitor rapamycin (100 nM) and evaluated changes in the autophagic biomarkers p62 and LC3B-II in JHU 011 and Cal27 wild
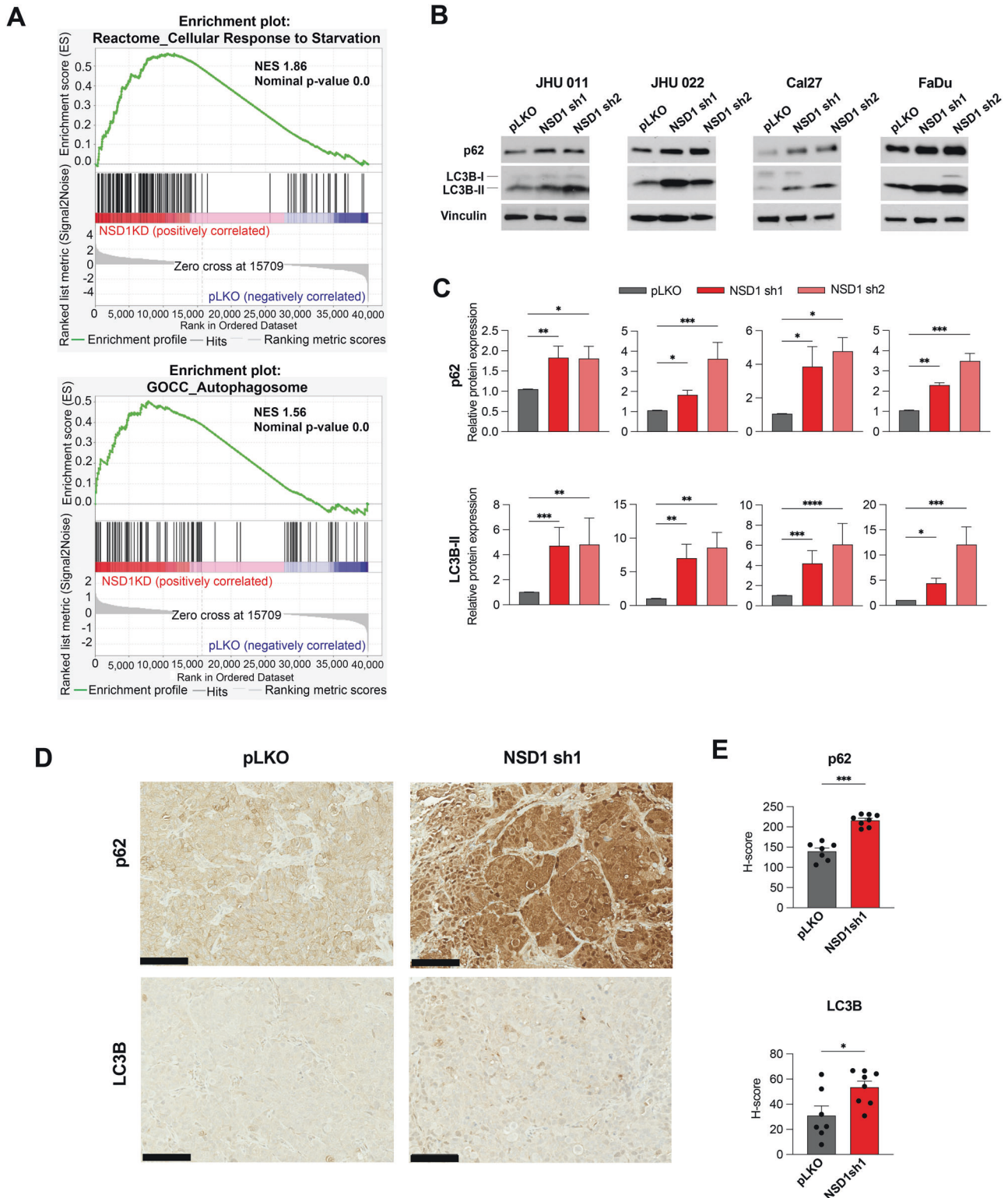
Fig. 2 NSD1 depletion leads to accumulation of p62 and LC3B-II proteins in HNSCC, suggesting autophagy disruption. A Normalized enrichment score (NES) for genes identified as part of the Reactome_Cellular Response to Starvation and GOCC_Autophagosome gene sets after GSEA of RNA-seq in JHU 011 and Cal27 cell lines. **B** Western blot of p62 and LC3B-II protein levels in JHU 011, JHU 022, Cal27, and FaDu cell lines upon doxycycline induction of NSD1 shRNA knockdown or pLKO control. **C** Quantification of western blot images in (**B**). Statistical significance was determined by Kruskal–Wallis with Dunn's multiple comparisons post-test. **D** Representative images for p62 and LC3B IHC staining in FaDu pLKO and NSD1sh1 tumors from the mouse xenograft models (20× magnification, scale bar 100 μm). **E** Quantification of average *H*-score from (**D**). Statistical significance was determined by Mann–Whitney test. Experiments were performed in at least three independent biological repeats. The error bars are presented as mean ± SEM. ns not significant, *$p < 0.05$, **$p < 0.01$, ***$p < 0.001$, and ****$p < 0.0001$.
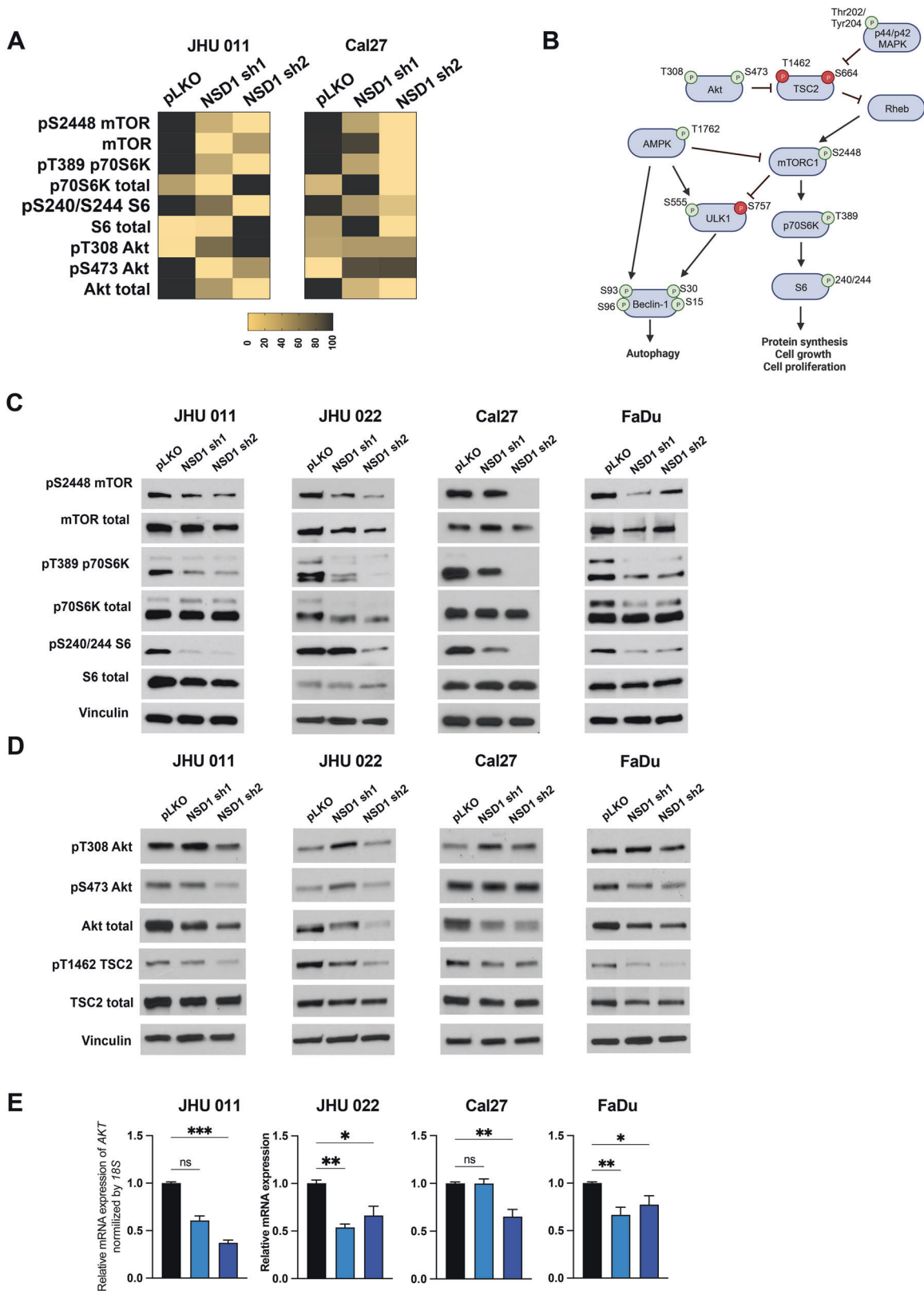
Fig. 3 Depletion of NSD1 inhibits Akt/mTORC1 signaling pathway. A A Heatmap of the RPPA results for JHU 011 and Cal27 cell lines. **B** Schema of Akt/mTORC1 signaling pathway. **C** Western blot of mTOR and its downstream target protein levels in HNSCC cell lines with induced NSD1 shRNA knockdown. **D** Western blot of Akt and its TSC2 protein levels in HNSCC cell lines with induced NSD1 shRNA knockdown. **E** mRNA expression of the *AKT* gene in HNSCC cell lines post doxycycline induction of pLKO control or NSD1 shRNA knockdown, as measured by qRT-PCR. *Akt* relative level was normalized to *18 S*, a control gene. Statistical significance was determined by Kruskal–Wallis with Dunn's multiple comparisons post-test. Experiments were performed in at least three independent biological repeats. The error bars are presented as mean ± SEM. ns not significant, *$p < 0.05$, **$p < 0.01$, ***$p < 0.001$, and ****$p < 0.0001$.

type cells. Rapamycin significantly reduced the level of pS2448 mTOR, confirming drug activity, and also its downstream targets in JHU 011 and Cal27 cell lines. In addition, we evaluated the p62 protein level, which serves as a link between LC3 and ubiquitinated substrates and protein level inversely correlates with autophagy activation [28].

Under conditions of only mTORC1 inhibition, HNSCC cells demonstrated a decrease in the p62 level (Supplementary Fig. S7A, B).

It is important to note that autophagy is a dynamic, multi-step process, and the increases in the level of LC3B-II can reflect the induction of autophagy or inhibition of fusion autophagosomes with lysosomes. The use of lysosomal protease inhibitors in
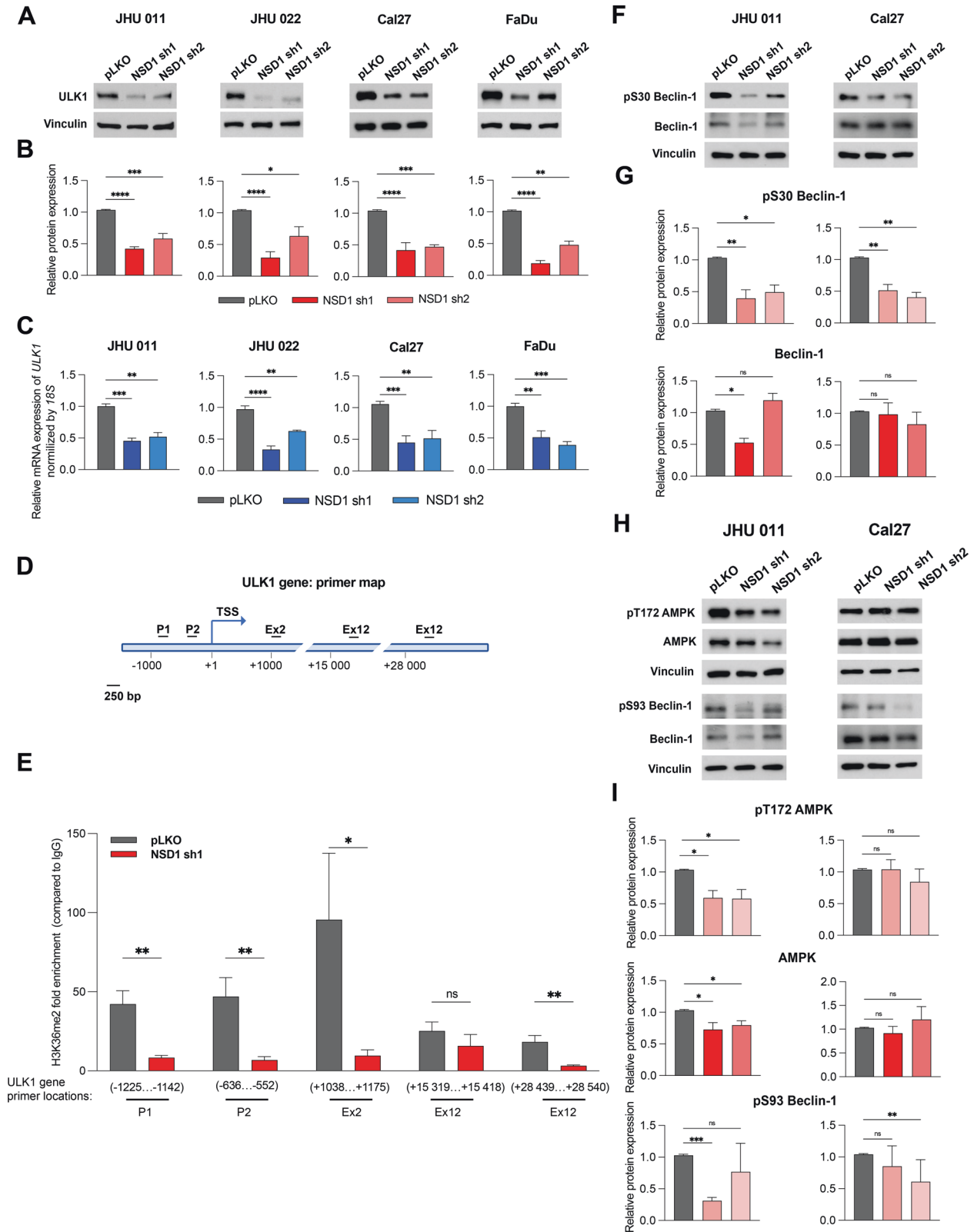
Fig. 4 NSD1 affects the initial stages of autophagy through the direct regulation of _ULK1_ gene expression in HNSCC. A Western blot of ULK1 protein level in JHU 011, JHU 022, Cal27, and FaDu cell lines upon doxycycline induction of NSD1 shRNA knockdown or pLKO control. **B** Quantification of Western blot in (**A**). Statistical significance was determined by Kruskal–Wallis with Dunn's multiple comparisons post-test. **C** mRNA expression of the _ULK1_ gene HNSCC cell lines post doxycycline induction of pLKO control or NSD1 shRNA knockdown, as measured by qRT-PCR. _ULK1_ relative level was normalized to _18 S_ as a control gene. Statistical significance determined by Kruskal–Wallis with Dunn's multiple comparisons post-test. **D** Primer location map of the _ULK1_ gene regions for CHIP-qPCR. P promoter, ex exon, TSS transcription start site. **E** ChIP-qPCR with H3K36me2 antibodies on the _ULK1_ gene. Statistical significance was determined by multiple Mann–Whitney test. **F** Western blot of pS30 Beclin-1 and Beclin-1 total protein levels in JHU 011 and Cal27 cell lines upon NSD1 knockdown upon doxycycline induction of NSD1 shRNA knockdown or pLKO control. **G** Quantification of Western blot in (**D**). Statistical significance was determined by Kruskal–Wallis with Dunn's multiple comparisons post-test. **H** Western blot of pT172 AMPK, AMPK total, pS93 Beclin-1, and Beclin-1 total protein levels in JHU 011 and Cal27 cell lines upon NSD1 knockdown upon doxycycline induction of NSD1 shRNA knockdown or pLKO control. **I** Quantification of Western blot in (**H**). Statistical significance was determined by Kruskal–Wallis with Dunn's multiple comparisons post-test. Experiments were performed in at least three independent biological repeats. The error bars are presented as mean ± SEM. ns not significant, $*p < 0.05$, $**p < 0.01$, $***p < 0.001$, and $****p < 0.0001$.

addition to mTOR inhibitors can help in an interpretation of autophagy and allow us to determine if an increase of LC3B-II is due to active autophagy flux or a decrease in the lysosome degradation [28]. We used as a protease inhibitor Chloroquine (CQ) in concentration 10 µM. The treatment of HNSCC cells by mTOR inhibitor, Rapamycin alone, has led to no visible changes in LC3B-II level, while the treatment of Rapamycin in combination with CQ demonstrated an increase in the level of LC3B-II, suggesting an activation of autophagy. In addition, the total level of ULK1, the kinase responsible for initial activation of autophagy, also has a trend to an increase upon treatment with rapamycin (Supplementary Fig. S7A, B). Reflecting on the fact that wild-type HNSCC cells demonstrate a decrease in p62 level and no visible changes by western blot in LC3B-II after mTORC1 inhibition alone, without CQ treatment, while NSD1-depleted cells have different profiles of p62, LC3B-II, and ULK1 protein levels, suggested that the effects we observe reflect an impaired autophagic flux upon NSD1 depletion.

To explore whether NSD1 knockdown leads to initiation of autophagy or a block in autophagic flux (autophagy degradative activity system), we transfected JHU 011 cell line wild type with pBabe-mCherry-EGFP-LC3B plasmid (Fig. 5A) and performed NSD1 knockdown using two different siRNA (Fig. 5B, C). We observed the increase in the percentage of yellow puncta (mCherry+EGFP+) in cells upon siNSD1 knockdown and, simultaneously, the decrease in free red puncta (mCherry+EGFP−), which suggests a decrease in autophagy flux efficiency (Fig. 5D, E). Taken together, these results suggest that NSD1 supports the autophagy degradation activity. Depletion of NSD1 has led to the accumulation of autophagosomes, which was observed by western blot (evidenced by accumulation of p62 and LC3B-II) and visualized by LC3B-tagged protein, suggesting disruption of autophagic flux.

DISCUSSION
In the past decades, NSD1/2/3 histone methyltransferases have been shown to play an important role in hematologic malignancies and solid tumors [8]. NSD1 is known to be oncogenic in leukemia, where NSD1 translocation drives a subset of acute myeloid leukemias with t(5;11)(q35;p15.5), which results in NUP98–NSD1 fusion protein [31]. The role of NSD1 in solid tumors is less well-established. In particular, while a subset of HPV-negative HNSCC, primarily laryngeal carcinoma with _NSD1_ loss-of-function mutations, has a favorable prognosis [9], this represents only a minority of HNSCC, while >80% HPV-negative head and neck tumors are _NSD1_-wild type. Interestingly, a recent Gameira et al. paper showed that while in HPV + HNSCC, NSD1/2/3 low expression cases associate with inferior outcomes, NSD1 and NSD2 high expressing HPV-negative HNSCC tumors show significant trends to associate with poor outcome [35]. Therefore, in this study, we tested the hypothesis that elevated levels of NSD1 may be oncogenic and could promote tumor progression in

HPV-negative HNSCC. We compared HNSCC cell growth in WT vs mutant cell lines, and the _NSD1_-mutant cell line with the lowest NSD1 expression levels was the slowest growing, suggesting that NSD1 may sustain HNSCC cell growth. Next, we used NSD1-expressing HNSCC (laryngeal, tongue/hypopharynx, HPV-negative models) cell lines to test an impact of depletion of NSD1 on cell growth. HNSCC cell lines demonstrated dramatically reduced growth upon NSD1 depletion in vitro, and also in vivo using xenografts.

Our data contrasts somewhat with a recently published study by Li et al., which showed that the immunocompetent allograft HNSCC mouse model does not demonstrate the difference between WT and NSD1-knockout tumor growth; the authors explain this effect by the ability of NSD1 to affect the tumor-immune microenvironment [19]. Additionally, it is certainly possible that mouse and human NSD1 roles in HNSCC could be different. Taken together, our findings in several independent HNSCC cell line models suggest that NSD1-expressing human HNSCC is dependent on NSD1 expression and suggests previously unsuspected oncogenic role for this enzyme in a large subset of HPV-negative HNSCC. Our findings complement advances in understanding the significance of H3K36 methyltransferases in HNSCC.

It was previously demonstrated that the NSD2 and NSD3, other members of NSD family proteins, have been implicated in HNSCC, and their loss leads to a decrease in cell viability [36, 37], but here, after studying NSD1, we find that this enzyme is also critical for HNSCC cell growth. Farhangdoost et al. recently demonstrated that CRISPR/Cas9-generated knockout of _NSD1_ as well as a mutation of _NSD1_ in HNSCC cell lines may downregulate several gene programs including mTORC1 signaling [11]. In our study, for the first time, we show the decrease of Akt/mTORC1 signaling in HNSCC, in response to NSD1 knockdown. While the regulation of mTORC1 and its downstream targets was at the level of phospho-isoforms changes, we found that the upstream activating effector of mTORC1, Akt, was reduced at both the total protein and transcriptional levels. However, to fully uncover the mechanism of this regulation it might be useful in the future to perform chromatin immunoprecipitation analyses to describe if this regulation occurs at the transcriptional level by NSD1 and K36me^2 dependent mechanisms.

Here, we performed RNA-seq in JHU 011 and Cal27 with NSD1 shRNA knockdown cell lines allowed us to further dissect mechanisms of HNSCC cell growth regulation by NSD1, and we found significant upregulation of starvation and autophagy-related gene expression programs. We suggested the autophagy is activated upon NSD1 knockdown in response to the mTORC1 pathway downregulation. Surprisingly, in the light of the fact that the activation of the gene program responsible for the for autophagosomes formation was upregulated after NSD1 knockdown, _ULK1_ gene was consistently positively regulated by NSD1 at both mRNA and protein levels. Some studies before described the
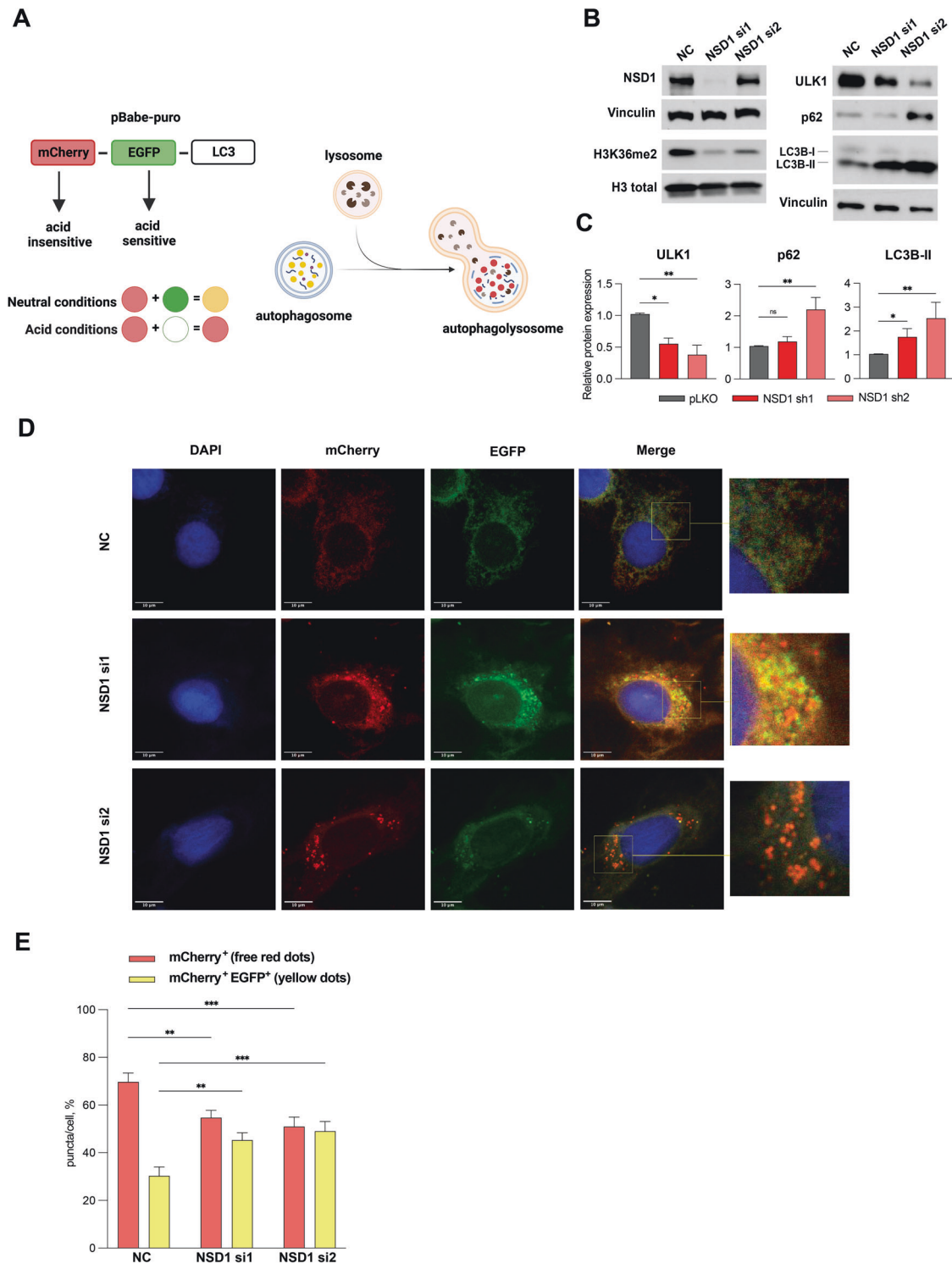
Fig. 5 Autophagic flux is disrupted in NSD1-depleted HNSCC cells. A Schema of the mCherry-GFP-LC3 reporter to monitor autophagic flux: pBabe-mCherry-EGFP-LC3B reporter where the GFP tag is acid-sensitive while the mCherry tag is acid-insensitive. That means, that at the higher level of autophagic flux, autophagosomes fuse with the lysosome (which has acid pH), and the intensity of the EGFP tag will die out, while at the low-level autophagic flux, both EGFP and mCherry tags will be detected and merged, resulting in yellow dots. **B** Western blot of NSD1, H3K36me^2, ULK1, p62, and LC3B protein levels upon siRNA knockdown or negative control (NC) siRNA at 72 h. **C** Quantification of western blot images in (**B**). Statistical significance was determined by Kruskal–Wallis with Dunn's multiple comparisons post-test. **D** Representative confocal images of JHU 011 cells transfected with the pBabe-puro-mCherry-EGFP-LC3B, and with siRNA knockdown of NSD1 that was induced during 72 h before cell fixation. Scale bars, 10 μm. **E** Quantification of puncta color percentage. Total number of autophagosomes (yellow) and autolysosomes (red) were quantified per cell ($n = 28$ cells/condition). Statistical significance was determined by ANOVA with Dunnett multiple comparison post-test. Each group was compared to negative control (NC). Experiments were performed in at least three independent biological repeats. The error bars are presented as mean ± SEM. ns not significant, *$p < 0.05$, **$p < 0.01$, ***$p < 0.001$, and ****$p < 0.0001$.
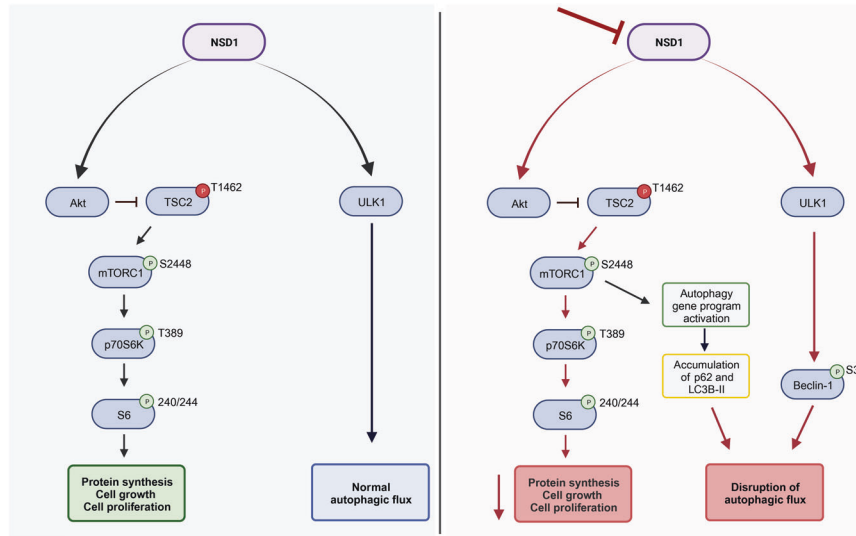
Fig. 6 Schema of the proposed working model.

epigenetic regulation of ULK1 by histone-methylation modifiers [38, 39]. Here, we showed that mechanistically, ULK1 expression is directly and positively regulated by NSD1 and K36me².

The increase in LC3B-II, along with accumulation of p62 protein in NSD1-depleted HNSCC cells indicates a failure to clear autophagosomes by fusion with the lysosomes. We confirmed autophagy defects by conducting autophagic flux experiments. Our observation of a significant decrease in the percentage of red fluorescence and increase in yellow fluorescence upon NSD1 depletion implies slowing down the autophagic flux. Taken together, decrease in Akt/mTORC1 activity and autophagy defects we observed suggests enhanced initiation of autophagy, which is ineffective in the absence of NSD1 (Fig. 6).

To our knowledge, NSD1/H3K36me² control of autophagy has never been described before and is a novel and interesting finding. Inhibition of autophagy in cancer remains an attractive field, and several autophagy inhibitors are being tested in clinical trials [40]. Similarly, Akt/mTOR pathways are important for the majority of HNSCC tumors because of several driver mechanisms, and clinical trials with agents targeting these pathways in HNSCC are ongoing [24, 41]. In summary, we conclude that the NSD1 enzyme is oncogenic and contributes to cancer cell growth in HPV-negative HNSCC via support of the Akt/mTORC1 pathway and regulation of autophagy. Inhibiting NSD1 enzyme and/or NSD1 downstream Akt/mTORC1 signaling, and to target/disrupt autophagy could be an exciting novel therapeutic strategy in HPV-negative HNSCC.

MATERIALS AND METHODS
Cell lines and cell culture
Human HNSCC cell lines FaDu, Cal27, SSC61, and SCC4 were obtained from the American Type Culture Collection (ATCC); JHU 011 and JHU 022 were gifts from Dr. E. Izumchenko (University of Chicago). A more detailed characterization of these cell lines is presented in Supplementary Table 1. HEK293T cells were used for retro- and lentivirus production. All cell lines were grown in RPMI-1640 with 10% FBS and 100 U/ml penicillin/streptomycin (Gibco). Cells were incubated in a 37 °C humidified incubator with 5% CO_2.

Vector construction and virus production
To generate stable cell lines with inducible NSD1 knockdowns, self-complementary single-stranded DNA oligos (Supplementary Table 2) were annealed and cloned into AgeI/EcoRI sites of Tet-pLKO-puro vector

(Addgene, #21915). Tet-pLKO-puro vectors were packaged into a lentivirus system with pCMV-VSV-G (Addgene, #8454) and psPAX2 (Addgene, #12260). A pBABE-puro mCherry-EGFP-LC3B plasmid was obtained from Addgene (#22418) and packaged into a retrovirus system with packing plasmid pCMV-VSV-G (Addgene, #8454) and pUMVC (Addgene, #8449). HEK293T cell line was used for retroviral and lentiviral system amplification with TransIT-293 Transfection Reagent (Mirus).

siRNA transfections
The sequences of siRNAs used for silencing *NSD1* and *ULK1* genes are shown in Supplementary Table 3; as a negative control we used siRNA Universal Negative Control #1 (SIC001, Sigma-Aldrich). Cells were plated onto 6-well plate for western blot or on glass coverslips for confocal microscopy. At 30% confluence cell were transfected with siRNAs at final concentrations of 20 nM using transfection agent TransIT-X2® Dynamic Delivery System (Mirus). Cells were lysed for western blot and/or fixed for confocal microscopy analysis and images acquisition, 72 hours post transfection.

Total RNA-sequencing and data analysis
Total RNA-seq. mRNA was extracted from JHU 011 and Cal27 cell lines with NSD1 knockdown (pLKO was used as a control), post 72 h of doxycycline induction. The stranded total RNA-seq was conducted at the Northwestern University NUSeq Core Facility. The Illumina Stranded Total RNA Library Preparation Kit was used to prepare sequencing libraries. The Kit procedure was performed without modifications. Illumina HiSeq 4000 Sequencer was used to sequence the libraries with the production of single-end, 50 bp reads.

RNA-seq analysis. The quality of reads in FASTQ format was evaluated using FastQC. Reads were trimmed to remove Illumina adapters from the 3′ ends using cutadapt [42]. Trimmed reads were aligned to the *human* genome using STAR [43]. Read counts for each gene were calculated using htseq-count [44] in conjunction with a gene annotation obtained from Ensembl (http://useast.ensembl.org/index.html). Normalization and differential expression were calculated using DESeq2 which employs the Wald test [45]. The cutoff for determining significantly differentially expressed genes was an FDR-adjusted *p*-value less than 0.05 using the Benjamini–Hochberg method.

GSEA (gene set enrichment analysis) software (https://www.gsea-msigdb.org/gsea/index.jsp) was used for gene pathway analysis using gene sets from Molecular Signatures Database v7.5.1.

RPPA analysis
JHU 011 and Cal27 cell lines with NSD1 shRNA knockdown (pLKO is as a control, NSD1 sh1, NSD1 sh2) were lysed and prepared according to MD

Anderson Core Facility instructions, as previously described, and RPPA was performed at the facility [46–48]. Analysis was performed using 487 antibodies. Data were visualized using the GraphPad Prism software.

Proliferation assay
In total, 500 cells/well were plated in 96-well cell culture plates in complete media. After 24 h, NSD1 knockdown was induced by 1 µg/ml of doxycycline. CellTiter-Blue® assay (Promega) reagent was added and incubated for 1.5 h, fluorescence was measured at 560/590 nm to obtain a 0 h time point. Next, the procedure was repeated at 72, 96, 120, 148, and 168 h. Proliferation was calculated as a relative value, where the 0 h time point was taken as a one.

Clonogenic assay
Cells were plated in 12-well plates (200 cells/well). After 24 h, NSD1 shRNA knockdown or pLKO (control) was treated with 1 µg/ml of doxycycline to induce knockdown. Then cells were incubated for 7–10 days at 37 °C, 5% CO_2 for colony formation. After 7–10 days, cells were fixed with 10% acetic acid/10% methanol solution and stained with 0.5% (w/v) crystal violet. Plates were scanned and colonies were counted using Image J software.

Apoptosis assay
Cells were seeded in a T-25 flask and NSD1 knockdown was induced for 144 h. Next, cells were trypsinized, prepared according to the manufacturer's protocol of the Alexa Fluor 488 Annexin V/Dead Cell Apoptosis Kit (Thermo Fisher Scientific), and analyzed using LSRFortessa Cell Analyzer (BD). At least 10,000 events were calculated for each sample.

RNA isolation and RT-qPCR
For total RNA isolation, Quick-RNA Miniprep Kit (Zymo research) was used according to the manufacturer's protocol. Complementary DNA was synthesized using iScript Reverse Transcription Supermix (Bio-Rad). Gene expression analysis was performed with QuantStudio 3 Real-Time PCR System (Applied Biosystem), using SYBR Green PCR master mix (Applied Biosystem); primer sequences are listed in Supplementary Table 4.

Western blot
Whole-cell lysates were extracted with lysis buffer (50 mM Tris pH 7.6, 2% SDS) with Halt Protease & Phosphatase Inhibitor Cocktail (Thermo Scientific). Protein concentrations were measured using Pierce BCA assay (Thermo Scientific). Separated proteins were transferred to the PVDF membrane. The membranes were blocked with 1% nonfat milk in TBST for 1 h at room temperature. After blocking, the membranes were incubated overnight at 4 °C with primary antibodies listed in Supplementary Table 5. Bands were developed using SuperSignal West Pico Plus Solution (Thermo Scientific) and detected with an autoradiography CL-Xposure Film (Thermo Scientific). Films were scanned, and images were quantified with Image J software.

Assessment of in vivo tumor growth
For in vivo tumor growth studies, 5×10^6 of FaDu cells with inducible NSD1 shRNA knockdown (FaDu pLKO is a control) were injected subcutaneously in the flank region of 7-week-old mice using CB17-SCID mice (Charles River), with 8 mice per each group. All animal procedures were done using institutionally approved animal protocol. After 5 days of tumor growth, when tumors volume reached 30–40 mm^2, mice have been started to feed with Doxycycline Rodent Diet (200 mg/kg, Bio-Serv) to induce shRNA knockdown. Tumors were measured every 5 days. Tumor volume was calculated with the formula: [volume = $0.52 \times$ (width)$^2 \times$ length]. After 25 days of the post-tumor cells injection, mice were euthanized, and tumor tissues were collected for histology and western blot.

Immunohistochemistry of mouse xenografts
Tumor tissues from mice were collected, fixed in 10% phosphate-buffered formaldehyde (formalin) for 36 h, and submitted to the Mouse Histology & Phenotyping Laboratory (MHPL) of Northwestern University. Samples were embedded in paraffin, and then hematoxylin and eosin (H&E) staining immunohistochemistry (IHC) was performed by using standard protocols. Antibodies for p62 and LC3B protein detection and their dilutions used for

IHC are listed in Supplementary Table 5. Slides were scanned, and the H-score was calculated using QuPath software (https://qupath.github.io/).

Tissue microarray construction and immunohistochemistry
Head and Neck surgical specimens resected at Northwestern Memorial Hospital, including were used to construct tissue microarrays (TMA). Clinical information (Supplementary Table 6) was available from the repository database and abstracted from clinical databases in an anonymized fashion (Northwestern IRB project # STU00214658, approved on 05/03/2021). The map of TMAs was created, reviewed, and constructed with the size of a 1.5 mm core by using the semi-automatic Veridiam Tissue Microarrayer VTA-100. Immunohistochemical studies were performed on 4-micron sections from Formalin-Fixed Paraffin Embedded (FFPE) TMA blocks on charged slides by using Leica Bond-Max Autostainer. Antibody dilutions used are listed in Supplementary Table 5. Stained slides were scanned using digital slide scanner Nanozoomer 2.0-HT (Hamamatsu); H-score was calculated using QuPath software (https://qupath.github.io/).

ChIP-qPCR
Approximately 3×10^7 cells were cross-linked with 1% formaldehyde. Chromatin immunoprecipitation (ChIP) assay was performed by using SimpleChIP Enzymatic Chromatin IP Kit (Cell Signaling Technology, #9003) according to the manufacturer's protocol. For immunoprecipitation, 2.5 µg of rabbit anti-H3K36me^2 antibody (Abcam, ab9049) was used per IP; the same amount of normal rabbit IgG antibodies were used as a control (CST, #2729) Purified DNA from immunoprecipitated chromatin was subjected to qPCR analysis using sing SYBR Green PCR master mix (Applied Biosystem). Primer sequences for ULK1 gene regions are listed in Supplementary Table 7. The results were calculated as a fold enrichment by normalizing on IgG control.

Autophagic flux measurement
Autophagy degradative activity (autophagic flux) was measured using an expression vector encoding the fusion protein mCherry-EGFP-LC3B (Addgene, #22418). We transfected the JHU 011 cell line with the pBabe-mCherry-EGFP-LC3B vector and established a stable cell line by puromycin selection. Cells were plated on the glass cover, and NSD1 was knocked down with siRNA for 72 h. Then, cells were fixed in 4% PFA for 20 min and mounted in ProLong Gold Antifade Reagent with DAPI (Invitrogen). Cells were visualized using a NIKON A1R (B) GaAsP confocal microscope fitted with a 100×, 1.4-NA objective in the presence of immersion oil. Images were analyzed in the Fuji software using the Analyze Particles plugin to calculate mCherry$^+$ and EGFP$^+$ single puncta and mCherry$^+$ EGFP$^+$ double-positive puncta. Puncta were quantified as a percent ratio per cell ($n = 28$ cells per condition).

Statistical methods
All used statistical analyses noted in the figure legends were performed and visualized using GraphPad Prism software (v.9.5.1).

DATA AVAILABILITY
Data presented in this study are available from the corresponding authors upon request.

REFERENCES
1. Johnson DE, Burtness B, Leemans CR, Lui VWY, Bauman JE, Grandis JR. Head and neck squamous cell carcinoma. Nat Rev Dis Prim. 2020;6:92.
2. Ferlay J, Colombet M, Soerjomataram I, Parkin DM, Pi¤eros M, Znaor A, et al. Cancer statistics for the year 2020: an overview. Int J Cancer. 2021;149:778–98.
3. Siegel RL, Miller KD, Wagle NS, Jemal A. Cancer statistics, 2023. CA Cancer J Clin. 2023;73:17–48.
4. American Society of Clinical Oncology. Head and Neck Cancer: Statistics 2023. https://www.cancer.net/cancer-types/head-and-neck-cancer/statistics.
5. Tumban E A. Current Update on Human Papillomavirus-Associated Head and Neck Cancers. Viruses. 2019;11.
6. Canning M, Guo G, Yu M, Myint C, Groves MW, Byrd JK, et al. Heterogeneity of the head and neck squamous cell carcinoma immune landscape and its impact on immunotherapy. Front Cell Dev Biol. 2019;7:52.

7. Husmann D, Gozani O. Histone lysine methyltransferases in biology and disease. Nat Struct Mol Biol. 2019;26:880–9.

8. Topchu I, Pangeni RP, Bychkov I, Miller SA, Izumchenko E, Yu J, et al. The role of NSD1, NSD2, and NSD3 histone methyltransferases in solid tumors. Cell Mol Life Sci. 2022;79:285.

9. Peri S, Izumchenko E, Schubert AD, Slifker MJ, Ruth K, Serebriiskii IG, et al. NSD1- and NSD2-damaging mutations define a subset of laryngeal tumors with favorable prognosis. Nat Commun. 2017;8:1772.

10. Papillon-Cavanagh S, Lu C, Gayden T, Mikael LG, Bechet D, Karamboulas C, et al. Impaired H3K36 methylation defines a subset of head and neck squamous cell carcinomas. Nat Genet. 2017;49:180–5.

11. Farhangdoost N, Horth C, Hu B, Bareke E, Chen X, Li Y, et al. Chromatin dysregulation associated with NSD1 mutation in head and neck squamous cell carcinoma. Cell Rep. 2021;34:108769.

12. Pan C, Izreig S, Yarbrough WG, Issaeva N. NSD1 mutations by HPV status in head and neck cancer: differences in survival and response to DNA-damaging agents. Cancers Head Neck. 2019;4:3.

13. Bui N, Huang JK, Bojorquez-Gomez A, Licon K, Sanchez KS, Tang SN, et al. Disruption of NSD1 in head and neck cancer promotes favorable chemotherapeutic responses linked to hypomethylation. Mol Cancer Therap. 2018;17:1585–94.

14. Lu T, Jackson MW, Wang B, Yang M, Chance MR, Miyagi M, et al. Regulation of NF-kappaB by NSD1/FBXL11-dependent reversible lysine methylation of p65. Proc Natl Acad Sci USA. 2010;107:46–51.

15. Zhang S, Zhang F, Chen Q, Wan C, Xiong J, Xu J. CRISPR/Cas9-mediated knockout of NSD1 suppresses the hepatocellular carcinoma development via the NSD1/H3/Wnt10b signaling pathway. J Exp Clin Cancer Res. 2019;38:467.

16. Chen Y, Li X, Xu J, Xiao H, Tang C, Liang W, et al. Knockdown of nuclear receptor binding SET domain-containing protein 1 (NSD1) inhibits proliferation and facilitates apoptosis in paclitaxel-resistant breast cancer cells via inactivating the Wnt/β-catenin signaling pathway. Bioengineered. 2022;13:3526–36.

17. He F, Xiao H, Cai Y, Zhang N. NSD1 promotes esophageal cancer tumorigenesis via HIF1α signaling. Cell Biol Toxicol. 2022;39:1835–50.

18. Brennan K, Shin JH, Tay JK, Prunello M, Gentles AJ, Sunwoo JB, et al. NSD1 inactivation defines an immune cold, DNA hypomethylated subtype in squamous cell carcinoma. Sci Rep. 2017;7:17064.

19. Li Y, Goldberg EM, Chen X, Xu X, McGuire JT, Leuzzi G, et al. Histone methylation antagonism drives tumor immune evasion in squamous cell carcinomas. Mol Cell. 2022;82:3901–18.e7.

20. Saloura V, Izumchenko E, Zuo Z, Bao R, Korzinkin M, Ozerov I, et al. Immune profiles in primary squamous cell carcinoma of the head and neck. Oral Oncol. 2019;96:77–88.

21. Laplante M, Sabatini DM. mTOR signaling in growth control and disease. Cell. 2012;149:274–93.

22. Molinolo AA, Hewitt SM, Amornphimoltham P, Keelawat S, Rangdaeng S, Meneses García A, et al. Dissecting the Akt/mammalian target of rapamycin signaling network: emerging results from the head and neck cancer tissue array initiative. Clin Cancer Res. 2007;13:4964–73.

23. Vander Broek R, Mohan S, Eytan DF, Chen Z, Van Waes C. The PI3K/Akt/mTOR axis in head and neck cancer: functions, aberrations, cross-talk, and therapies. Oral Dis. 2015;21:815–25.

24. Marquard FE, Jücker M. PI3K/AKT/mTOR signaling as a molecular target in head and neck cancer. Biochem Pharmacol. 2020;172:113729.

25. Kim YC, Guan KL. mTOR: a pharmacologic target for autophagy regulation. J Clin Invest. 2015;125:25–32.

26. Mathew R, Karantza-Wadsworth V, White E. Role of autophagy in cancer. Nat Rev Cancer. 2007;7:961–7.

27. Topchu IA, Tikhomirova MV, Bulatov ER, Abramova ZI, Boumber YA. Knockout of the histone methyltransferase NSD1 leads to a decrease in cell proliferation and an increase in sensitivity to cisplatin in laryngeal squamous cell carcinoma. Sib J Oncol. 2023;22:76–84.

28. Klionsky DJ, Abeliovich H, Agostinis P, Agrawal DK, Aliev G, Askew DS, et al. Guidelines for the use and interpretation of assays for monitoring autophagy in higher eukaryotes. Autophagy. 2008;4:151–75.

29. Lamb CA, Yoshimori T, Tooze SA. The autophagosome: origins unknown, biogenesis complex. Nat Rev Mol Cell Biol. 2013;14:759–74.

30. Lucio-Eterovic AK, Singh MM, Gardner JE, Veerappan CS, Rice JC, Carpenter PB. Role for the nuclear receptor-binding SET domain protein 1 (NSD1) methyltransferase in coordinating lysine 36 methylation at histone 3 with RNA polymerase II function. Proc Natl Acad Sci USA. 2010;107:16952–7.

31. Wang GG, Cai L, Pasillas MP, Kamps MP. NUP98–NSD1 links H3K36 methylation to Hox-A gene activation and leukaemogenesis. Nat Cell Biol. 2007;9:804–12.

32. Park JM, Seo M, Jung CH, Grunwald D, Stone M, Otto NM, et al. ULK1 phosphorylates Ser30 of BECN1 in association with ATG14 to stimulate autophagy induction. Autophagy. 2018;14:584–97.

33. Qian X, Li X, Cai Q, Zhang C, Yu Q, Jiang Y, et al. Phosphoglycerate kinase 1 phosphorylates beclin1 to induce autophagy. Mol Cell. 2017;65:917–31.e6.

34. Kim J, Kim YC, Fang C, Russell RC, Kim JH, Fan W, et al. Differential regulation of distinct Vps34 complexes by AMPK in nutrient stress and autophagy. Cell. 2013;152:290–303.

35. Gameiro SF, Ghasemi F, Zeng PYF, Mundi N, Howlett CJ, Plantinga P, et al. Low expression of NSD1, NSD2, and NSD3 define a subset of human papillomavirus-positive oral squamous carcinomas with unfavorable prognosis. Infect Agents Cancer. 2021;16:13.

36. Saloura V, Cho H-S, Kiyotani K, Alachkar H, Zuo Z, Nakakido M, et al. WHSC1 promotes oncogenesis through regulation of NIMA-related kinase-7 in squamous cell carcinoma of the head and neck. Mol Cancer Res. 2015;13:293–304.

37. Saloura V, Vougiouklakis T, Zewde M, Kiyotani K, Park JH, Gao G, et al. WHSC1L1 drives cell cycle progression through transcriptional regulation of CDC6 and CDK2 in squamous cell carcinoma of the head and neck. Oncotarget. 2016;7:42527–38.

38. Byun S, Seok S, Kim YC, Zhang Y, Yau P, Iwamori N, et al. Fasting-induced FGF21 signaling activates hepatic autophagy and lipid degradation via JMJD3 histone demethylase. Nat Commun. 2020;11:807.

39. Ma X, Wang Q. Short-chain fatty acids attenuate renal fibrosis and enhance autophagy of renal tubular cells in diabetic mice through the HDAC2/ULK1 axis. Endocrinol Metab (Seoul). 2022;37:432–43.

40. Mohsen S, Sobash PT, Algwaiz GF, Nasef N, Al-Zeidaneen SA, Karim NA. Autophagy agents in clinical trials for cancer therapy: a brief review. Curr Oncol. 2022;29:1695–708.

41. Lenze N, Chera B, Sheth S. An evaluation of buparlisib for the treatment of head and neck squamous cell carcinoma. Expert Opin Pharmacother. 2021;22:135–44.

42. Martin M. Cutadapt removes adapter sequences from high-throughput sequencing reads. EMBnet.journal. 2011;17:3.

43. Dobin A, Davis CA, Schlesinger F, Drenkow J, Zaleski C, Jha S, et al. STAR: ultrafast universal RNA-seq aligner. Bioinformatics. 2013;29:15–21.

44. Anders S, Pyl PT, Huber W. HTSeq-a Python framework to work with high-throughput sequencing data. Bioinformatics. 2015;31:166–9.

45. Love MI, Huber W, Anders S. Moderated estimation of fold change and dispersion for RNA-seq data with DESeq2. Genome Biol. 2014;15:550.

46. Iadevaia S, Lu Y, Morales FC, Mills GB, Ram PT. Identification of optimal drug combinations targeting cellular networks: integrating phospho-proteomics and computational network analysis. Cancer Res. 2010;70:6704–14.

47. Kornblau SM, Tibes R, Qiu YH, Chen W, Kantarjian HM, Andreeff M, et al. Functional proteomic profiling of AML predicts response and survival. Blood. 2009;113:154–64.

48. Tibes R, Qiu Y, Lu Y, Hennessy B, Andreeff M, Mills GB, et al. Reverse phase protein array: validation of a novel proteomic technology and utility for analysis of primary leukemia specimens and hematopoietic stem cells. Mol Cancer Ther. 2006;5:2512–21.

COMPETING INTERESTS
The authors declare no competing interests.

ADDITIONAL INFORMATION

Supplementary information The online version contains supplementary material available at https://doi.org/10.1038/s41420-024-01842-6.

Correspondence and requests for materials should be addressed to Yanis Boumber.

Reprints and permission information is available at http://www.nature.com/reprints

Publisher's note Springer Nature remains neutral with regard to jurisdictional claims in published maps and institutional affiliations.